Sensors and Actuators B 143 (2009) 76–86

Contents lists available at ScienceDirect

Sensors and Actuators B: Chemical

journal homepage: www.elsevier.com/locate/snb

Spectral, amplitude and phase sensitivity of a plasmonic gas sensor in a metallic photonic crystal slab geometry: Comparison of the near and far field phase detection strategies

Lina Shi [a], Andrei Kabashin [a,b], Maksim Skorobogatiy [a,*]

[a] École Polytechnique de Montréal, Génie Physique, C.P. 6079, succ. Center-Vile Montreal, Québec H3C3A7, Canada[1]
[b] Laboratoire Lasers, Plasmas et Procédés Photoniques (LP3 UMR 6182 CNRS), Faculté des Sciences de Luminy, Université de Méditerranée, Case 917, 13288 Marseille, France

ARTICLE INFO

Article history:
Received 25 February 2009
Received in revised form 19 August 2009
Accepted 20 September 2009
Available online 2 October 2009

Keywords:
Surface plasmon resonance
Phase sensitive detection
Gas sensors

ABSTRACT

Using finite-difference time-domain method, we investigate phase and amplitude reflective properties of a metallic photonic crystal slab comprising a two-dimensional array of gold disks placed on top of a thin gold film resting on a dielectric substrate. Photonic crystal slab overcladding is a gaseous analyte. Throughout the paper we discuss prospectives of application of such photonic crystal slabs to sensing of changes in the gas refractive index. We start by studying the field distributions and spectral positions of two types of surface plasmons supported by such PhCs as a function of the photonic crystal lattice period, the gold film thickness, and the gold disk size. First, we find that the spectral positions of plasmon peaks depend almost linearly on the photonic crystal lattice constant, which is a manifestation of the delocalized nature of a plasmon extending over the PhC lattice. This is possible due to connectivity between metallic disks via an underlying thin metallic film. Second, we find that the width of plasmonic peaks is highly sensitive to the relative size of the metallic disks compared to the lattice period. This can be well explained via interaction between the localized plasmons situated at the disc edges in the adjacent unit cells. We therefore find that plasmons in the metallic PhC slabs featuring metallic discs connected by a metallic film exhibit both strong local and non-local properties. Third, we find that, generally, there are two types of plasmons supported by such metallic PhCs. One type is a plasmon with a large fraction of its field located in the gas overcladding, which is most suitable for sensing. In contrast, another plasmon type has its field concentrated at the interface between a thin metal film and a substrate; such plasmons are only weakly sensitive to the refractive index of the sensor overcladding, and, therefore, can serve as convenient references for the sensor measurements. Finally, we report sensor sensitivities to changes in the real part of the gas refractive index when using amplitude and phase-based detection strategies. We start by demonstrating that when measured in the sensor far field, the phase sensitive detection provides much lower detection limit (1.8×10^{-6} RIU) compared to that of the amplitude-based detection (1.5×10^{-4} RIU). We then find that sensor phase and amplitude sensitivities can be considerably enhanced when performing measurements using point detectors placed in the near field of a sensor. Particularly, we have established that both phase and amplitude sensitivities are maximal when measured in the sensor near field along the normal to the sensor surface going through the point of the highest symmetry of a photonic crystal unit cell (Γ point). Sensor resolution as high as 2.2×10^{-7} RIU for the phase-based detection and 7.4×10^{-5} RIU) for the amplitude-based detection are found, with the most dramatic enhancement observed for the phase detection approach. We believe that experimental verification of the sensor sensitivity enhancement using phase detection in the sensor near field can be accomplished by using scanning near-field optical microscopy.

1. Introduction

The ability to detect small amounts of gases is important in many fields such as environmental protection, security, industrial process control, meteorology, etc. Currently, there are several types of commercial gas sensors available, including, catalytic calorimetric sensors, electrochemical sensors and optical sensors. Among all the gas sensors, optical sensors remain the most accurate and

* Corresponding author.
E-mail address: maksim.skorobogatiy@polymtl.ca (M. Skorobogatiy).
[1] http://www.photonics.phys.polymtl.ca.

0925-4005/$ – see front matter © 2009 Elsevier B.V. All rights reserved.
doi:10.1016/j.snb.2009.09.036

reliable as they do not rely on inherently noisy catalytic or electrochemical interactions. The most common optical gas sensors are the absorption spectroscopy-based sensors. Such gas sensors typically measure changes in the wavelength resolved transmission through the volume of a gas sample. In other words, they measure imaginary part of the gas refractive index. Presence and concentration of the specific gases is then quantified through the strength of the specific absorption lines in the gas spectrum (typically located in the infrared (IR) spectral region). The main advantage of a spectroscopic approach is that it is a rather general one, applicable to a broad variety of gases. The main disadvantage of spectroscopic sensors is that they tend to be bulky, complex, and expensive due to the necessity of long gas cells to enhance absorption, as well as due to the use of expensive IR detectors and high resolution spectrometers.

In order to create compact, robust (and potentially low-cost) gas sensors, various photonic crystal-based (PhC) sensor designs were recently proposed [1–4]. In contrast to absorption spectroscopy, PhC-based sensors typically measure changes in the real part of the analyte refractive index. This is achieved through detection of spectral shifts in some resonant features of the photonic crystals, such as transmission or reflection peaks. In a stark contrast to absorption spectroscopy, PhC-based sensors in their bare configuration are, generally, not selective to a particular type of gas. Indeed, as the real part of a gas refractive index typically exhibits only a weak spectral dispersion, there are no sharp features (such as specific absorption peaks) that one can use to differentiate one gas from another. To achieve selectivity of such sensors one typically functionalizes the sensor surface with the nanolayers of gas recognition elements (such as polymers, or inorganic compounds). Such elements provide sensor specificity by selectively binding only a specific type of gas molecules. Finally, gas concentration is quantified by measuring changes in the refractive index of a recognition layer. Spectral sensitivities as high as $S_\lambda = \Delta\lambda/\Delta n = 433$ nm/RIU (nanometer/refractive index unit) were demonstrated [4] using all-dielectric photonic crystals-based sensors. Sensitivity figure quoted above defines spectral shift of a resonant peak given by $\Delta\lambda$ when the analyte refractive index changes by Δn. Making a reasonable assumption that 0.1 nm spectral shift can be reliably resolved with a low-cost spectrometer system, such sensitivity defines a detection limit of 2.3×10^{-4} RIU. Although sensitivity of photonic crystal-based sensors is already quite high, lower detection limits are always desirable, especially for the applications in security and environmental control.

Recently, surface plasmon resonance (SPR)-based sensors have attracted significant attention due to their record sensitivities and low noise levels. Propagating at the metal/dielectric interface, surface plasmons [5] are extremely sensitive to changes in the refractive index of the dielectric. This feature constitutes the core of many SPR sensors. Typically, these sensors are implemented in the Kretschmann–Raether prism geometry where a p-polarized light is launched through a glass prism and reflected from a thin metal (Au, Ag) film deposited on the prism facet [6]. The presence of a prism allows phase matching of an incident electromagnetic wave with a plasmon wave at the metal/dielectric analyte interface at a specific combination of the angle of incidence and wavelength. Since plasmon excitation condition depends resonantly on the value of the refractive index of an analyte medium within 100–300 nm from the interface, the method enables, for example, detection, with unprecedented sensitivity, of biological binding events on the metal surface [7]. The course of a biological reaction can then be followed by monitoring angular [7,8], spectral [9] or phase [10,11] characteristics of the reflected light. Typical sensitivity of a SPR sensor in the bulk prism configuration is $\sim 5 \times 10^3$ nm/RIU [12] for aqueous analytes (refractive index ~1.33), with a corresponding sensor resolution of $\sim 2 \times 10^{-5}$ RIU. Spectral sensitivity as high as $\sim 3 \times 10^4$ nm/RIU was reported at 690 nm [13], with a corresponding sensor resolution of $\sim 3.3 \times 10^{-6}$ RIU; that is to say, SPR sensors are the most sensitive among all the optical sensors. Moreover, advanced detector design and processing electronics can be used to push the detection limit of a Kretschmann configuration to as low as 1×10^{-8} RIU [14]. SPR sensor technology has been commercialized and SPR biosensors have become an important tool for characterizing and quantifying biomolecular interactions.

To date, most of the SPR sensors employ a bulky prism geometry. In this respect SPR sensors based on the periodic metallic nano- and micro-arrays are very interesting as they offer high degree of miniaturization, while still retaining high sensitivity. In particular, SPR sensing of biochemicals using nano-hole arrays was recently described in [15–17]. In a typical implementation of such a sensor, a square lattice of sub-wavelength holes is etched into a thin metal film. When a plane wave is incoming onto such a slab, enhanced transmission through the sub-wavelength hole array is obtained. This is generally attributed to the resonant excitation of surface plasmon waves [18]. Resonant frequency of such a plasmon wave is highly sensitive to the material parameters of a metal slab and surrounding material, which is a principal reason for utilizing such resonances for sensing. Practically, sensing in such systems is performed in the transmission mode via detection of the spectral shifts in the peak positions for small changes in the analyte refractive index. As an example, Tetz et al. [16] obtained sensitivities of 1022 nm/RIU at the operation wavelength of 850 nm. Principal disadvantage of an SPR sensor employing an array of sub-wavelength holes is that the measurements are performed in transmission mode. In such an interrogation regime transmitted intensities, even at their maximum, are greatly reduced compared to the intensity of an incoming light. This greatly reduces the sensor dynamic range.

In this paper, we study a gas sensor design based on a metal PhC slab comprising a monolayer of gold disks placed on top of a gold film on a glass substrate (see Fig. 1). Such a sensor is conveniently interrogated in the reflection mode perpendicular to its surface. At resonance, incoming plane wave is almost completely absorbed at the metal surface due to coupling to plasmons, while out of resonance the light is almost completely reflected, thus leading to a high dynamic range of a sensor. We then characterize sensitivity of such a sensor to changes in the refractive index of a gas surrounding the metal PhC slab. Moreover, we find that metallic PhC slabs can also support a plasmon confined to the metal film/substrate interface, and, thus, insensitive to the changes in the analyte refractive index. Such a resonance can be used as a natural reference during measurements to improve sensor sensitivity and simplify data collection and interpretation.

Moreover, we find that in the vicinity of a resonance, phase of a reflected signal exhibits strong variation. We further demonstrate that this can be exploited to increase sensor sensitivity by several orders of magnitude compared to the case of amplitude-based detection. We also present detailed simulations of the phase behavior as a function of the various design parameters and find that, generally, the phase sensitivity increases for stronger localized plasmons. Finally, we find that phase sensitivity of a sensor can be considerably enhanced when placing a detector in the near field of a test structure at certain symmetry points of an underlying photonic crystal lattice. We call thus registered phase as “nano-phase” in contrast to a traditional phase which is usually registered in the far field. We believe that experimental measurement of such a phase can be performed using scanning near-field optical microscopy.

Our work is organized as follows. In Section 2 we detail our design and simulation method. The effects of the lattice period, the film thickness and the disk size are presented in Sections 3–5, respectively. Section 6 is devoted to the amplitude and phase sensitivity of the metallic PhC slab sensors. And the sensitivities at near and far field are compared in Section 7.

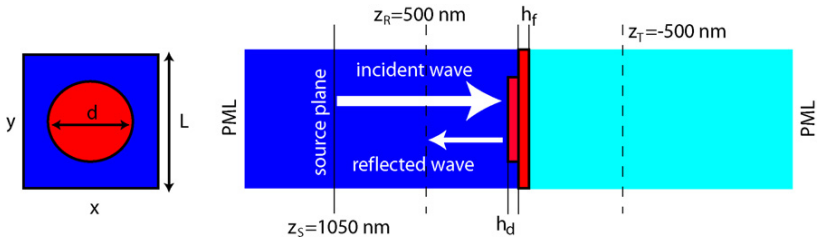

Fig. 1. Schematic of a metallic PhC slab-based SPR sensor. Sensor comprises a square array of the h_d-high gold disks placed on top of a h_f-thick gold film on a semi-infinite glass substrate. Disk diameter and lattice constant are comparable to the operation wavelength ~600 nm. The cyan, red and blue, respectively, denote a substrate, gold and a gas. Incident planewave is propagating along z direction. (For interpretation of the references to color in this figure legend, the reader is referred to the web version of the article.)

2. Simulation method and model

Sensor geometry that we model comprises a two-dimensional array of gold disks of height h_d placed on top of a gold film of thickness h_f, which, in turn, is deposited on top of a semi-infinite glass substrate with refractive index $n_s = 1.52$ (BK7 glass) (Fig. 1). The disk diameter d and the lattice period L are comparable to the wavelength of operation. Simulations are performed using the Meep [19] implementation of the finite-difference time-domain (FDTD) method. Fig. 1 shows schematic of the computation domain. In all our simulations reflection spectra were computed for the normal angle of incidence. The cyan, red and blue, respectively, denote a substrate, gold and a gas. The dielectric function for gold is approximated using the Drude–Lorentz formula [20]:

$$\epsilon_{DL}(\omega) = \epsilon_\infty - \frac{\omega_D^2}{\omega(\omega + i\gamma_D)} - \frac{\Delta\epsilon \cdot \Omega_L^2}{(\omega^2 - \Omega_L^2) + i\Gamma_L\omega} \quad (1)$$

where $\epsilon_\infty = 5.9673$, the plasma frequency $\omega_D = 2\pi \cdot 2.1136 \times 10^{15}$ Hz, the damping coefficient $\gamma_D = 2\pi \cdot 1.592 \times 10^{13}$ Hz, the oscillator strength $\Omega_L = 2\pi \cdot 6.5007 \times 10^{14}$ Hz, the spectral width of the Lorentz oscillators $\Gamma_L = 2\pi \cdot 1.0486 \times 10^{14}$ Hz and the weighting factor $\Delta\epsilon = 1.09$.

The computational domain is a single unit cell shown in Fig. 1. At the faces of a unit cell which are perpendicular to the z direction we impose the perfectly matched layer (PML) absorbing boundary conditions. At the remaining four faces, we impose periodic boundary conditions. The structure is excited by a Gaussian pulse source (in time) centered around a frequency of interest having a spatial distribution in the form of a planewave. Incoming planewave propagates in the air region along z direction. Center of coordinates (0,0,0) is in the center of a unit cell. $z = 0$ defines position of the interface between the gold discs and a gold film. The electric field of a source is polarized along x direction. The elementary grid size is 5 nm × 5 nm × 5 nm in space, and the time step is 0.0083 fs to guarantee numerical stability of simulations. Extent of a unit cell in z direction is 3 μm. Extent of a unit cell in the x and y directions is a lattice period L. The monitor plane for reflection is located $z_R = 500$ nm from the interface between the gold disks and a gold film. Source plane is located $z_S = 1050$ nm from the same interface. The monitor surface for transmission is located $z_T = -500$ nm from the above mentioned interface. In all our simulations the pulse propagated completely through the unit cell after 417 fs. In order to get the normal-incidence reflection coefficient (the reflected flux divided by the incident flux), we perform two simulations, one with and another without the metal PhC slab (for the details of the method see the Meep manual [19] and Appendix A).

3. Effect of the lattice period

We start by presenting the effect of lattice period on excitation of the surface plasmon resonances in a metallic PhC slab. In

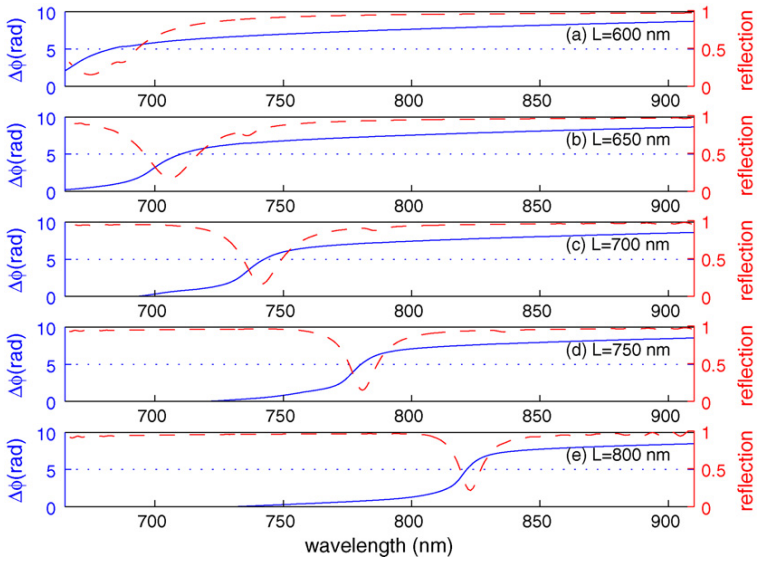

Fig. 2. Phase (solid blue) and reflection spectra (dash red) of the metallic PhC slab for various values of the lattice constant $L = 600$, 650, 700, 750, and 800 nm. The gold disk diameter is $d = 465$ nm, the disk height is $h_d = 50$ nm, and the gold film thickness is $h_d = 55$ nm. (For interpretation of the references to color in this figure legend, the reader is referred to the web version of the article.)

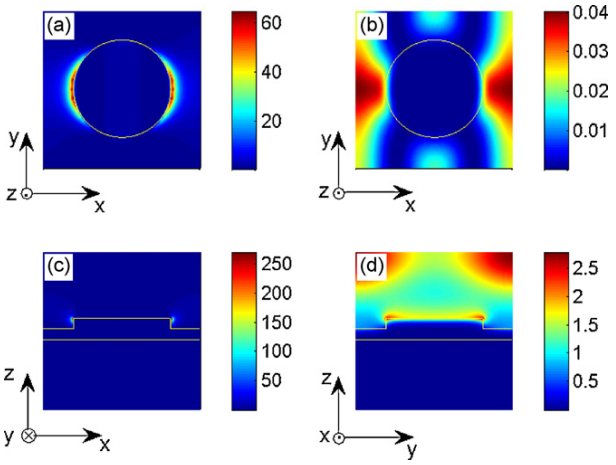

Fig. 3. Distribution of the electric field intensity $|E_x|^2$ in the vicinity of a metal film at the wavelength of a plasmon resonance 780.9 nm for $L = 750$ nm in Fig. 2. (a) *xy* plane located 5 nm above the upper surface of the gold disk (inside a gas). (b) *xy* plane located 5 nm below the lower surface of the gold film (inside a substrate). (c) *xz* plane cut through the center of the gold disk. (d) *yz* plane cut through the center of the gold disk.

Fig. 2 we present the reflectance (dash red) evaluated at the plane $z_R = 500$ nm, and phase (solid blue) evaluated at the point (0, 0, 500) of the metallic PhC slab. The PhC under study comprised the 465 nm diameter gold disks positioned on top of a thin metallic film in a square array configuration with lattice constants $L =$ 600, 650, 700, 750, and 800 nm. The disk height and the metallic film thickness are $h_d = 50$ nm and $h_f = 55$ nm, respectively. In Fig. 2 the reflection spectra and phase display several distinct trends. Namely, (i) All the spectra exhibit plasmon resonance with a peak center wavelength linearly proportional to the value of the lattice constant L. By increasing the lattice constant, plasmonic resonance is shifted towards longer wavelengths. At the center wavelength of a plasmon resonance, reflection is minimal. (ii) The phase curve becomes steeper and the width of a plasmon resonance narrows as the lattice constant increases.

Center wavelength of a plasmon resonance is clearly sensitive to the value of a lattice period, indicating that phase matching between an incoming wave and a plasmon mode is achieved through the interaction with a lattice. Particularly, amplitudes of the reciprocal lattice vectors reduce when the lattice constant increases $|\mathbf{G}| \sim 1/L$. The amplitude of a surface plasmon wavevector propagating on a flat metal film reduces for longer wavelengths $|\mathbf{k}_{pl}| \sim n_{eff}^{pl}/\lambda_{pl}$. As it is the reciprocal wavevector that is responsible for the phase matching between the in-plane plasmon and the normally incident planewave $|\mathbf{k}_{pl}| \simeq |\mathbf{G}|$, one expects that plasmon resonance wavelength should shift to longer wavelengths when the lattice period increases $\lambda_{pl} \sim n_{eff}^{pl} L$.

To understand better the structure of a plasmon mode, in Fig. 3 we present a snapshot in time of the electric field intensity distribution $|E_x|^2$ in the vicinity of a gold film at the wavelength of a plasmonic resonance 780.9 nm for the lattice constant $L =$ 750 nm. In particular, four field distributions are presented: in the *xy* plane 5 nm above the upper surface of the gold disk (inside a gas) (Fig. 3(a)), in the *xy* plane 5 nm below the lower surface of the gold film (inside a substrate) (Fig. 3(b)), in the *xz* plane (Fig. 3(c)) and in the *yz* (Fig. 3(d)) plane cut through the center of the gold disk. To ease interpretation of the presented field distributions we remind the reader that the incoming planewave is polarized in such a way as to contain only the E_x component of the electric field.

From Fig. 3 one can see how the plasmons can exhibit the properties of both long-range and localized plasmons. Indeed from Fig. 3(a) and (c) we see that most of the plasmon energy is strongly localized at the edges of a metallic disk, and from this point of view, the plasmons are highly localized. On the other hand, from Fig. 3(b) and (d) we see that plasmons also have some non-negligible fields extended across the whole unit cell along *xy* direction and localized in *z* direction at the metal film/air interface.

From Fig. 3 we can also understand why the width of a plasmon peak decreases when the lattice period increases. Particularly, as the plasmon fields are strongly localized at the disk edges, in this respect, the overall plasmon mode of a disk array can be considered as made of the localized plasmons weakly interacting with each other through the field overlap across the boundaries of the adjacent unit cells. As it is well known from the theory of coupled resonator arrays, a narrow eigenstate of a single resonator will be broadened in the resonator array, and such broadening increases with increased interaction between the individual resonators. Therefore, when increasing the lattice period, individual disks will be placed further apart, thus leading to weaker interaction between the plasmons localized at the edges of adjacent disks. As a consequence, reduced interaction between the plasmons localized at the individual disks will lead to the narrower resonant states of a disk array.

Notably, the sharpness of a phase change near the wavelength of plasmon excitation decreases with the width of a plasmon peak.

4. Effect of the metal film thickness

In this section we study effect of the gold film thickness on plasmonic resonances. Fig. 4 shows the reflectance spectra (dash red) and phase (solid blue) of five metal PhC slabs, each having a gold film of different thickness $h_f = 25, 35, 45, 55$, and 65 nm. In these simulations we take $L = 750$ nm, $h_d = 50$ nm. With increasing thickness of the metal film the position of the main plasmonic peak is virtually independent of the film thickness as plasmon field is concentrated at the disk upper edge facing the gas.

A remarkable feature found in Fig. 4 is the appearance of a second spectral dip (at ~840 nm) in the reflection spectra. When changing the refractive index of gas from $n_a = 1.00$ to $n_a = 1.05$ (we only present the two reflection spectra for $h_f = 25$ nm case in Fig. 4(a)), position of the second resonance peak is practically unchanged (in stark contrast to the behavior of the main plasmonic resonance peak). Such a stationary resonant feature in the reflection spectrum can be used as a natural reference that can simplify considerably the sensor data acquisition and data interpretation. In the following we establish the physical nature of the dip by looking at the distribution of the electric field intensity $|E_x|^2$ in the various planes cut through the unit cell. Particularly, in Fig. 5 we present a snapshot of the field intensity distributions for the wavelength of 846.3 nm and the gold film thickness of $h_f = 25$ nm. Fig. 5(a) shows field intensity distribution in the *xy* plane located 5 nm above the upper surface of the gold disk (inside a gas). Fig. 5(b) shows field intensity distribution in the *xy* plane located 5 nm below the lower surface of the gold film (inside a substrate). Fig. 5(c) and (d) show field intensity distributions in the *xz* (Fig. 5(c)) and *yz* (Fig. 5(d)) planes cut through the center of the gold disk.

From the field intensity distributions in Fig. 5 it is clear that the second resonant dip in the reflection spectrum of Fig. 4 corresponds to the excitation of a plasmon propagating at the interface between the gold film and a substrate. As most of the field in such a plasmon is concentrated in the substrate it is not surprising that such an excitation is only weakly sensitive to the value of the gas overcladding refractive index. Finally, we note that the excitation wavelength of a plasmon extended into a substrate (second dip) is higher than the excitation wavelength of a plasmon extended into a gas (first dip). This is easy to rationalize by noting that the

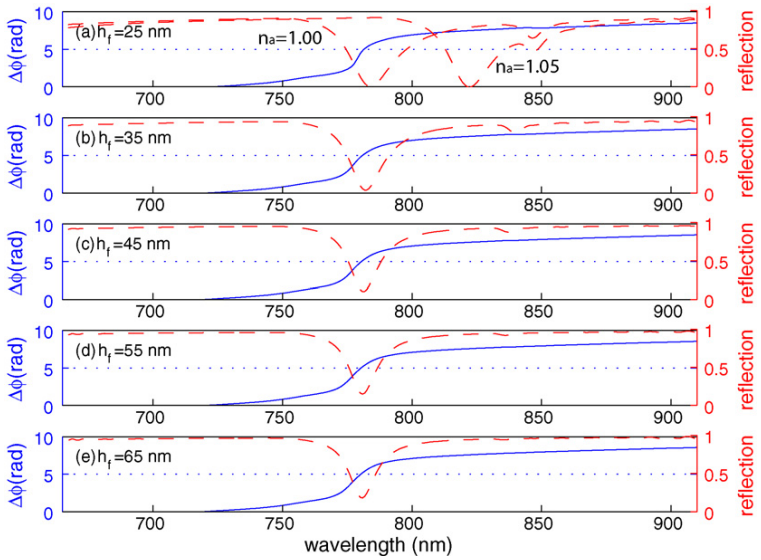

Fig. 4. Phase (solid blue) and reflection spectra (dash red) of the metallic PhC slab for various thicknesses of the gold film $h_f = 25$, 35, 45, 55, and 65 nm. The lattice constant is $L = 750$ nm, the gold disk height is $h_d = 50$ nm, and the gold disk diameter is $d = 465$ nm. (For interpretation of the references to color in this figure legend, the reader is referred to the web version of the article.)

effective refractive index $n_{eff}^{pl,s}$ of a "substrate" plasmon is close to that of a substrate, and, therefore, larger in value than the effective refractive index $n_{eff}^{pl,g}$ of a "gas" plasmon which is close to that of a gas. If it is the same reciprocal lattice wavevector **G** that is responsible for the phase matching between the normally incident planewave and the two different plasmons, from the dispersion relation it follows that $|\mathbf{G}| \simeq n_{eff}^{pl,s}/\lambda_{pl,s} \simeq n_{eff}^{pl,g}/\lambda_{pl,g}$, and, therefore, $\lambda_{pl,s}/\lambda_{pl,g} \simeq n_{eff}^{pl,s}/n_{eff}^{pl,g} > 1$.

From Fig. 5 it is also clear that the phase is only weakly sensitive to the thickness of the metal film.

5. Effect of the disk size

We now investigate the effect of the disk size on surface plasmon resonance. In this section, the gold film thickness is fixed at $h_f = 35$ nm. Fig. 6(a)–(c) shows the reflection spectra (dash red) and phase (solid blue) of the three metallic PhC slabs having the gold disks with diameters $d = 310$, 465, and 620 nm and height 50 nm. Fig. 6(d)–(f) shows the reflection spectra (dash red) and phase (solid blue) of the three metallic PhC slabs incorporating the gold disks with heights $h_d = 35$, 55, and 75 nm and diameter 465 nm.

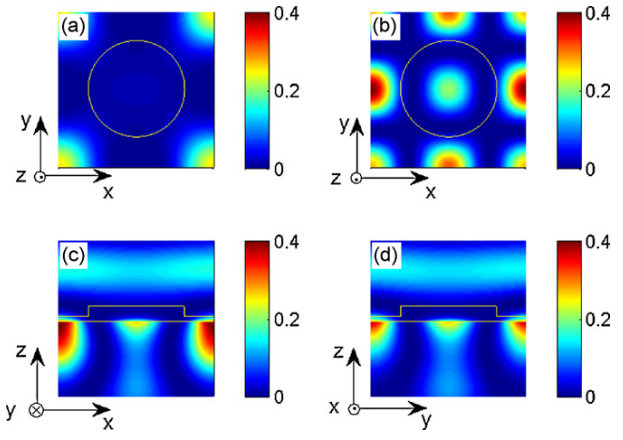

Fig. 5. Distribution of the electric field intensity $|E_x|^2$ in the vicinity of a metal film at the wavelength of the second plasmon resonance 846.3 nm for $h_f = 25$ nm in Fig. 4. (a) *xy* plane 5 nm above the upper surface of the gold disk (inside a gas). (b) *xy* plane 5 nm below the lower surface of the gold film (inside a substrate). (c) *xz* plane cut through the center of the gold disk. (d) *yz* plane cut through the center of the gold disk.

From Fig. 6 we note that positions of the plasmon peaks are only weakly sensitive to the variation in the disk height and disk diameter. In contrast, peak width increases substantially when either the disk diameter or the disk height is increased. Broadening of the resonance peaks in the case of larger disk diameters (lattice constant is fixed) can be rationalized by the stronger inter-cell interaction between the individual plasmons localized at the adjacent disks (for more details see the section on the effect of a lattice constant). This is due to the geometrical fact that plasmons are localized at the disk edges, while the disk edges in the adjacent unit cells become closer when the disk diameter increases. As a consequence, this leads to stronger field overlap and interaction between the localized plasmons and, hence, spectral broadening of the eigenstates of a disk array.

Similarly, to the results of Section 3, phase change as a function of the wavelength is sharper for the spectrally narrow plasmonic peaks.

6. Sensor performance using amplitude response of the metallic PhC slabs

In the prior sections we studied spectrally resolved reflection and phase changes as a function of the various structural parameters of metallic PhC slabs. In particular, we have demonstrated that the choose of a larger lattice constant or the smaller disk size results in spectrally narrower plasmonic peaks and steeper phase variation. In contrast, the thickness of a gold film has only weak effect on the resonance peak shape, while effective somewhat stronger the position of a "substrate" plasmonic peak.

As indicated in the abstract and Section 1 of the paper, one of the important applications of metallic PhC slabs can be sensing of the refractive index changes in gaseous analytes. In this section

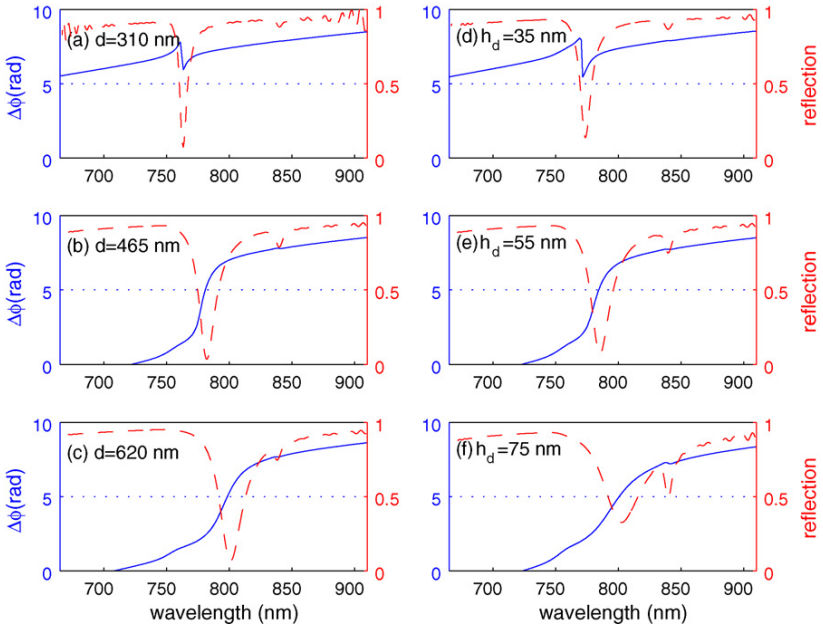

Fig. 6. The phase (solid blue) and the reflection spectra (dash red) of the metallic PhC slab for different geometrical parameters of the gold disks. The lattice period is $L = 750$ nm, the gold film thickness is $h_f = 35$ nm. (a–d) The disk height is $h_d = 50$ nm. The disk diameters are, respectively, $d = 310$, 465, and 620 nm. (e–h) The disk diameter is $d = 465$ nm. The disk heights are, respectively, $h_d = 35$, 55, and 75 nm. (For interpretation of the references to color in this figure legend, the reader is referred to the web version of the article.)

we investigate in more details sensitivity of several representative structures presented earlier in the paper.

As the first approach to sensing with metallic PhC slabs we consider spectral detection method. Within the framework of this method one first acquires a reflection (or transmission) spectrum for a certain known analyte with a known refractive index. At the same time, one also records spectral positions of the resonant peaks. One then repeats the procedure for a test analyte, extracts positions of the new resonant peaks, and compares them to the positions of the same resonant peaks for a known analyte. Given individual spectral sensitivities of the resonant peaks used in detection, one can then infer the unknown value of test analyte refractive index. Spectral sensitivities of the individual peaks are typically inferred from the calibration measurements, where the refractive index of a known analyte is varied controllably and resonant peak positions are recorded. Theoretically, spectral sensitivities of the individual peaks can be evaluated by computing reflection spectra for different values of the analyte refractive index, and then by dividing the value of change in the spectral position of a peak by the value of change in the refractive index of analyte. As an example, in Fig. 4(a) two reflection spectra are computed for the $n_a = 1.00$ and $n_a = 1.05$ values of the analyte refractive index. Sensitivity of the main plasmonic peak can then be computed as $S = (822.1 - 784.2)/0.05\,\text{nm/RIU} = 758\,\text{nm/RIU}$. Assuming that 0.1 nm change in the position of a spectral peak can be detected reliably, sensor resolution becomes 1.3×10^{-4} RIU. Main disadvantage of a spectral detection method is the necessity of performing high resolution spectral scans, which typically require expensive equipment and take considerable time for the data acquisition.

Here we discuss two other strategies for detecting changes in the gas refractive index. These are the amplitude-based detection method and the phase-based detection method. In the amplitude-based detection method, all the measurements are performed at a single wavelength corresponding to the wavelength of maximal amplitude sensitivity. Defining $R(\lambda, n_a)$ to be the reflection spectrum for the n_a value of the analyte refractive index, the amplitude sensitivity is defined as

$$S_R(\lambda, n_a) = \lim_{\Delta n \to 0} \frac{R(\lambda, n_a + \Delta n) - R(\lambda, n_a)}{\Delta n}. \quad (2)$$

The maximum sensitivity is, typically, achieved at the wavelength of maximum slope in the reflection spectrum. Main advantage of this method is that all the measurements are performed at a single wavelength, which is generally located in the visible spectral range where inexpensive sources and detectors are readily available. Note that as sensitive response occurs only in the wavelength region where the plasmon absorption peak appears, therefore, even within amplitude-based sensing approach a calibration scan is required to actually find such a peak. Such a calibration scan, however, is only required once when the sensor is manufactured, while during sensor operation no scans are necessary. Moreover, position of a resonance peak is typically set by the sensor design, therefore acquisition of a full spectral response of a sensor is only needed as a post-fabrication step to verify sensor compliance with the manufacturing specks. All this is not to say that data interpretation from the amplitude-based sensors is easier or that the amplitude-based sensors are more reliable than sensors using a full spectral acquisition. In fact, because of the single wavelength operation, amplitude-based sensor range is typically limited only to small changes in the analyte refractive index. Moreover, without a full spectral scan it is challenging to distinguish noise in the sensor reading due to, say, temperature variation versus small change in the analyte refractive index.

As an example of the amplitude-based sensor consider metallic PhC slab with the following parameters $d = 465$ nm, $h_d = 35$ nm, $h_f = 35$ nm, $L = 750$ nm. Reflection spectrum of such a sensor is presented in Fig. 7(a). To find amplitude sensitivity we use definition (2), where the two required reflection spectra are calculated for $n_a = 1$ and $n_a + \Delta n = 1.0001$. Resultant amplitude sensitivity as a function of wavelength is presented in Fig. 7(b). The maximum of the amplitude sensitivity is achieved at the wavelength 775.1 nm, at which $S_R(\lambda, n_a = 1) = 67\,\text{RIU}^{-1}$. Making an experimentally reasonable assumption that standard detectors and electronics can

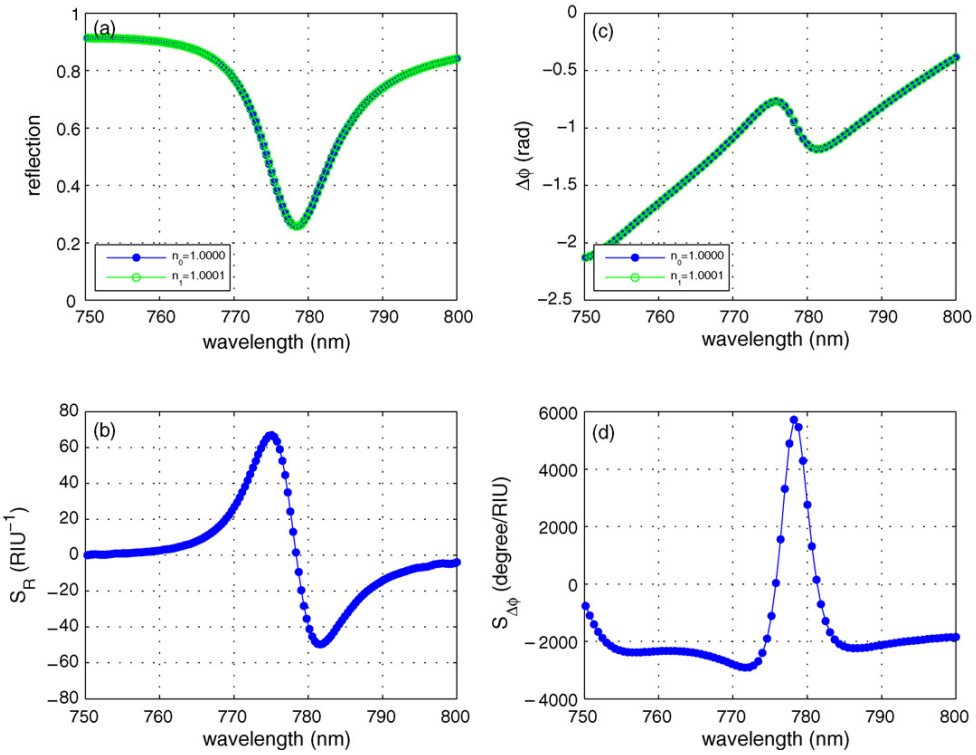

Fig. 7. Amplitude and phase response of the metallic PhC slab sensor with the gold film thickness $h_f = 35$ nm, the gold disk height $h_d = 35$ nm, the gold disk diameter $d = 465$ nm, and the lattice constant $L = 750$ nm. (a) Reflection spectra for $n_a = 1$. (b) Amplitude sensitivity of a sensor for small variations in the gas refractive index. (c) Phase response of the sensor for $n_a = 1$. (d) Phase sensitivity of a sensor for small variations in the gas refractive index.

reliably resolve 1% variations in the reflection coefficient, we arrive at the sensor resolution of 1.5×10^{-4} RIU.

7. Sensor performance using far field phase response of the metallic PhC slabs

In this section, we present a detection method based on the measurement of phase changes in the reflected wave. To date, phase-based detection is the most sensitive compared to the spectral and amplitude-based ones. Phase sensitive detection currently constitutes a very active research topic and is detailed in many publications [10,11,21–37]. Within phase sensitive method, one detects changes in the interference pattern created by the wave reflected form a sensor and the reference wave. Moreover, near resonant features, such as plasmon resonance peaks, phase of the reflected wave exhibits especially rapid variation and high sensitivity to the value of a measurand. Overall, detection of phase allows much higher resolution when compared to the amplitude-based and spectral-based methods. In what follows we present the computational approach for the simulation of the phase response of a sensor using FDTD method and the results of simulations.

To get the phase of the reflected wave we run two simulations, one is a full simulation with the sensor structure, the other one is a simulation with an empty computational cell, while otherwise identical boundary conditions and excitation source. In both simulations a particular component of the electromagnetic field (E_x in our case) is recorded as a function of time at a fixed point in space (x, y, z). At the end of simulations, one has two time histories for the field components, one is for the full simulation $f(t)$, and another one is for the reference (incoming) wave $f_0(t)$. We then Fourier transform the reflected wave component $(f(t) - f_0(t))$, as well as the reference wave component $f_0(t)$ to find the single frequency contributions $T_0(\omega) = fft(f_0(t))$, $T_R(\omega) = fft(f(t) - f_0(t))$. Finally, the phase of the reflected wave is calculated as

$$\phi = \arctan \frac{\mathrm{Im}(T_R(\omega)/T_0(\omega))}{\mathrm{Re}(T_R(\omega)/T_0(\omega))}. \tag{3}$$

In Fig. 7(c) we present phase $\phi(\lambda, n_a)$ of the reflected wave as a function of wavelength, assuming $n_a = 1$. The phase is detected at the point which is 1800 nm from the gold film/disk interface (that is the point (0, 0, and 1800 nm)). As will be explained in the next chapter, this separation from the PhC guarantees phase detection in the far field regime as it is typically the case in the actual experiment. Note that near the wavelength of plasmonic resonance 778.2 nm the phase exhibits rapid variation. To find phase sensitivity we use definition similar to (2). Particularly, in the vicinity of the $n_a = 1.00$ value of the gas refractive index, the phase sensitivity is defined as

$$S_\phi(\lambda, n_a) = \lim_{\Delta n \to 0} \frac{\phi(\lambda, n_a + \Delta n) - \phi(\lambda, n_a)}{\Delta n}. \tag{4}$$

In our simulations, the two required phase spectra in (4) are calculated for $n_a = 1.0000$ and $n_a + \Delta n = 1.0001$. Resultant phase sensitivity as a function of wavelength is presented in Fig. 7(d). The maximum of phase sensitivity is achieved at the wavelength 778.2 nm, at which $S_\phi(\lambda, n_a = 1) = 5.7 \times 10^3$ degree/RIU. Making an experimentally reasonable assumption that standard detectors and electronics can reliably resolve phase variation $\Delta\phi \sim 0.01^\circ$, we arrive at the sensor resolution of 1.8×10^{-6} RIU.

8. Enhancement of the phase sensitivity using near-field phase response of the metallic PhC slabs

In the previous sections we have presented phase response of various sensors for which point detector was placed in the sensor far field. In this respect, a particular choice of the position of

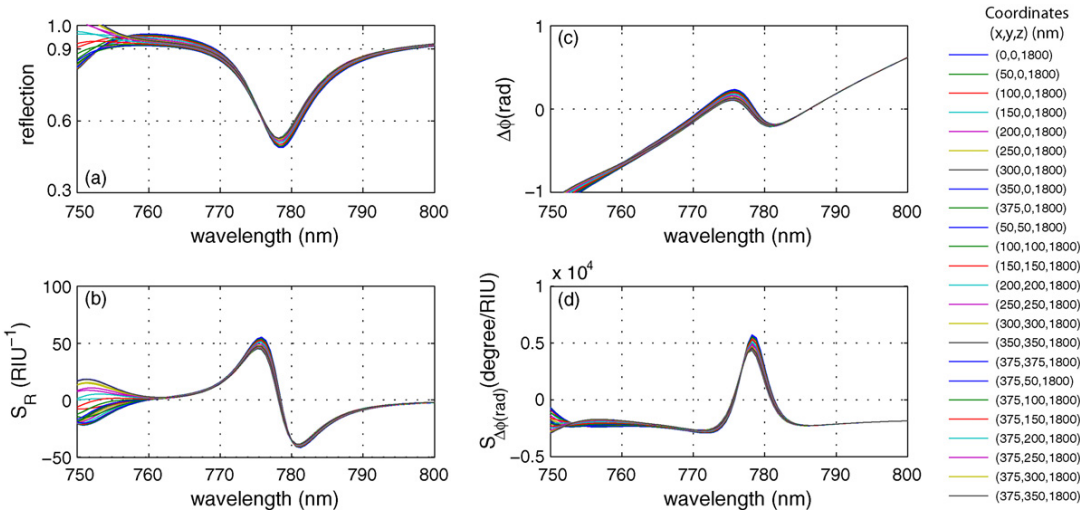

Fig. 8. Amplitude and phase response of the metallic PhC slab sensor with the gold film thickness $h_f = 35$ nm, the gold disk height $h_d = 35$ nm, the gold disk diameter $d = 465$ nm, and the lattice constant $L = 750$ nm. Different curves correspond to the different positions of a point detector in the monitor plane $z_R = 1800$ nm located in the sensor far field. Coordinates of the point detector in the unit cell of a PhC are presented on the right in (nm). (a) Reflection spectra for $n_a = 1$. (b) Amplitude sensitivity of a sensor for small variations in the gas refractive index. (c) Phase response of the sensor for $n_a = 1$. (d) Phase sensitivity of a sensor for small variations in the gas refractive index.

a point detector in the unit cell of a PhC was not important (this is confirmed later in this section). At the same time, we have also presented amplitude response of a sensor, where detector was in the form of an infinite monitor surface, therefore an averaged over the PhC unit cell sensor response was reported.

In this last section, we study dependence of the phase and amplitude sensitivities of a metallic PhC-based sensor as a function of the spatial location of a point detector. It is natural to expect that the measured signal will be different at different points in the PhC unit cell, therefore the related phase and amplitude sensitivities can be also different. Particularly interesting question is how sensor sensitivity differs when measured in the near field versus far field of a sensor. Experimentally, point detection can be realized using scanning near-field optical microscopy.

In Figs. 8 and 9 we present reflection spectra with corresponding amplitude sensitivity, as well as spectrally resolved phase dependence and phase sensitivity of the metallic PhC slab with the following parameters: $d = 465$ nm, $h_d = 35$ nm, $h_f = 35$ nm, $L =$

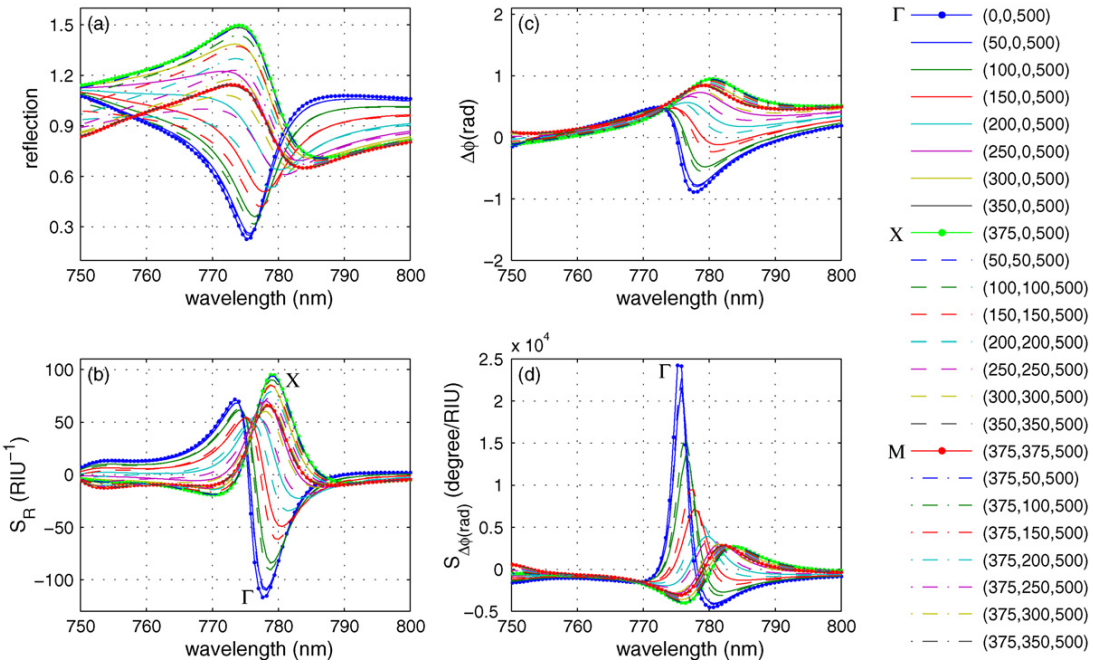

Fig. 9. Amplitude and phase response of the metallic PhC slab sensor with the gold film thickness $h_f = 35$ nm, the gold disk height $h_d = 35$ nm, the gold disk diameter $d = 465$ nm, and the lattice constant $L = 750$ nm. Different curves correspond to the different positions of a point detector in the monitor plane $z_R = 500$ nm located in the sensor near field. Coordinates of the point detector in the unit cell of a PhC are presented on the right in (nm). (a) Reflection spectra for $n_a = 1$. (b) Amplitude sensitivity of a sensor for small variations in the gas refractive index. (c) Phase response of the sensor for $n_a = 1$. (d) Phase sensitivity of a sensor for small variations in the gas refractive index.

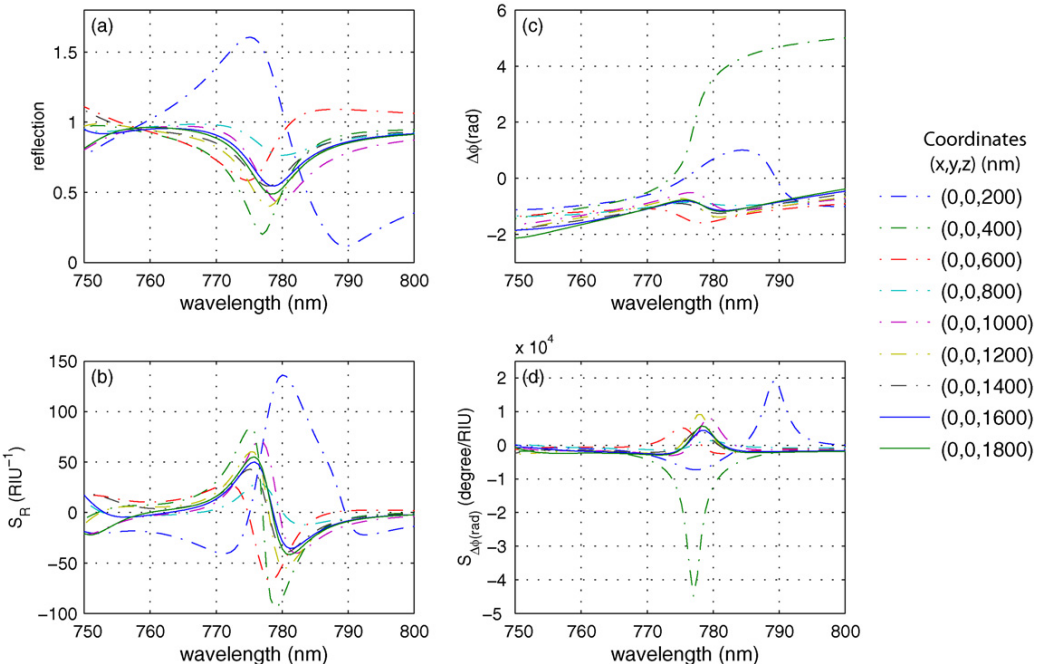

Fig. 10. Amplitude and phase response of the metallic PhC slab sensor with the gold film thickness $h_f = 35$ nm, the gold disk height $h_d = 35$ nm, the gold disk diameter $d = 465$ nm, and the lattice constant $L = 750$ nm. Different curves correspond to the different elevations of a point detector above the plane of a PhC at the Γ point of a unit cell. (a) Reflection spectra for $n_a = 1$. (b) Amplitude sensitivity of a sensor for small variations in the gas refractive index. (c) Phase response of the sensor for $n_a = 1$. (d) Phase sensitivity of a sensor for small variations in the gas refractive index.

750 nm. Different curves correspond to different observation points in the two monitor planes located in the near and far field of a sensor. Particularly, in Fig. 8 results are presented for the monitor plane in the sensor far field $z_R = 1800$ nm above the sensor surface. Note that in the far field (Fig. 8), amplitude and phase responses of a sensor are essentially independent of the position of a point detector in the monitoring plane. In fact, it is the insensitivity of the sensor performance to the position of the observation point that allows us to claim that the monitor plane is in the far field of a sensor. The amplitude sensitivity of a sensor with a detector located in the far field is found to be 50 RIU^{-1}; such a sensitivity defines sensor resolution of 2×10^{-4} RIU assuming that 1% variation in the intensity can be detected reliably. Phase sensitivity of a sensor with a detector located in the far field is found to be 5×10^3 degree/RIU; such a sensitivity defines sensor resolution of 2×10^{-6} RIU assuming that $\Delta\phi \sim 0.01^\circ$ variation in the phase can be detected reliably.

In Fig. 9 results are presented for the monitor plane in the sensor near field $z_R = 500$ nm above the sensor surface. In stark contrast to sensor performance in the far field, in the near field sensor sensitivity depends strongly on the position of a point detector. Further analysis (see Fig. 9(a) and (b)) shows that the phase sensitivity (4) is maximal for the point detector located in the center of a unit cell (Γ point in Fig. 9). Maximal amplitude sensitivity is also registered by the point detector located at the Γ point, while there is also a local maximum for the amplitude sensitivity for a detector located in the middle of the edge of a unit cell (X point). The maximal amplitude sensitivity is found to be 117 RIU^{-1}; such a sensitivity defines sensor resolution of 8.6×10^{-5} RIU assuming that 1% variation in the intensity can be detected reliably. Maximal phase sensitivity is found to be 2.5×10^4 degree/RIU; such a sensitivity defines sensor resolution of 4×10^{-7} RIU assuming that $\Delta\phi \sim 0.01^\circ$ variation in the phase can be detected reliably.

From Figs. 8 and 9 we can see that when operating in the sensor near field, considerable enhancement in both the amplitude and phase sensitivities of a sensor can be achieved compared to the far field operation.

Finally, Fig. 10 shows sensor amplitude and phase sensitivities for various elevations of a point detector above the surface of a PhC slab at the Γ point of a unit cell ($(x, y) = (0, 0)$). Observe that amplitude sensitivity is enhanced by as much as a factor of 3, while phase sensitivity is enhanced by as much as a factor of 8 for sensors operating in the near field compared to the far field operation. In our simulations the maximal amplitude sensitivity of 136.2 RIU^{-1} was found for a point detector located $z_R = 200$ nm above the sensor surface (Γ point), with a corresponding sensor resolution 7.4×10^{-5} RIU. The maximal phase sensitivity of 4.5×10^4 degree/RIU was found for a point detector located $z_R = 400$ nm above the sensor surface (Γ point), with the corresponding sensor resolution of 2.2×10^{-7} RIU. When moving further away from the sensor surface, the sensitivities decrease, while achieving some constant value in the far field.

9. Conclusion

Using finite-difference time-domain method, we investigated surface plasmon resonances in the metallic photonic crystal slabs. We then studied amplitude and phase characteristics of sensors based on metal PhC slabs for detecting changes in the gas refractive index. The gas sensor considered in this work comprised a two-dimensional array of gold disks on top of a gold film, which, in turn, was deposited on a glass substrate. The sensor overcladding was a gaseous analyte. The sensor was interrogated under normal incidence in the reflection mode. Excitation of the two plasmon types was observed in such a sensor. One plasmon type is an excitation confined to the edge of the gold disks with its fields penetrating strongly into the analyte overcladding. Such a plasmon was then used for gas detection. Another plasmon type is an excitation confined to the interface between the gold film and a substrate with very limited penetration of the plasmon fields into analyte.

Such a plasmon can be used as a reference to simplify spectral detection.

Finally, both the far field and near field detection was studied and significant enhancement of the sensor sensitivity was found when near field detection was used. First, amplitude detection and phase detection were studies assuming either planar or point detectors placed in the far field of a sensor (1.8 μm above the sensor surface). The corresponding sensor resolutions were independent of the position of a point detector in the observation plane and they were found to be 1.5×10^{-4} RIU for the amplitude-based detection, and 1.8×10^{-6} RIU for the phase detection. When operated in the near field (< 0.5 μm above the sensor surface) a significant enhancement of the sensor sensitivity was found for both the amplitude and phase detection strategies. Thus, resolution of a sensor using amplitude-based detection was found to be 7.4×10^{-5} RIU when operating 200 nm above the sensor surface, while resolution of a sensor using phase-based detection was found to be 2.2×10^{-7} RIU when operating 400 nm above sensor surface. Finally, maximal resolution was always found along the normal to the sensor surface going through the point of highest symmetry of a PhC unit cell (Γ point).

Acknowledgements

This work is supported in part by the Canada Institute for Photonic Innovations grant FP3, Canada Research Chair Program, and NSERC Strategic grant "Miniaturized Si-based plasmonics platform for gas detection."

Appendix A.

Calculation of the reflection coefficients closely follow the Meep manual [19].

For a harmonic wave of frequency ω, transmitted power is given by the integral of a Poynting vector over the monitor plane $z = z_T$ in the substrate (source plane is in the gas overcladding):

$$P_T(\omega) = \hat{\mathbf{z}}\mathrm{Re}\int \mathbf{E}_\omega(x, y, z_T) \times \mathbf{H}_\omega(x, y, z_T)\, dx\, dy. \quad (5)$$

One starts by launching a short pulse. One then accumulates the Fourier transforms $\mathbf{E}_\omega$ and $\mathbf{H}_\omega$ for a set of points in the monitor plane by using direct summation over the time. For example, for the electric field:

$$\mathbf{E}_\omega(x, y, z_T) = \frac{dt}{\sqrt{2\pi}} \sum_{j=0}^{j=j_{max}} e^{i\omega dtj}\mathbf{E}(x, y, z_T, t). \quad (6)$$

Simulation ends when no more field is left in the computational cell (criterium for the choice of j_{max}). One then computes frequency dependent flux $P_T(\omega)$ according to (5) by using Fourier components (6) of the electromagnetic fields. Finally, to calculate transmission coefficient one performs an additional normalization simulation with a uniform unit cell filled only with gas (no sensor). By repeating the steps outlined above one then finds normalization flux $P_T^0(\omega)$, which finally allows to compute transmission coefficient as $T = P_T(\omega)/P_T^0(\omega)$.

If the monitor plane for reflection is located in-between the source plane and a sensor, to compute reflection coefficient one has to separate the incoming and reflected fluxes crossing the monitor plane. Thus, for a harmonic wave of frequency ω, reflected power is given by the integral of a Poynting vector over the monitor plane $z = z_R$ as

$$P_R(\omega) = \mathrm{Re}\int [\mathbf{E}_\omega(x, y, z_R) - \mathbf{E}_\omega^0(x, y, z_R)] \times [\mathbf{H}_\omega(x, y, z_R) - \mathbf{H}_\omega^0(x, y, z_R)]\, dx\, dy, \quad (7)$$

where $\mathbf{E}_\omega^0(x, y, z_R)$ and $\mathbf{H}_\omega^0(x, y, z_R)$ are the incoming electric and magnetic fields computed using a uniform computational cell filled with gas (no sensor).

Alternatively, for a point detector, reflection or transmission coefficients are defined using the same (5) and (7), however without performing integrations over the monitor surfaces.

References

[1] T.M. Geppert, S.L. Schweizer, J. Schilling, C. Jamois, A.V. Rhein, D. Pergande, R. Glatthaar, P. Hahn, A. Feisst, A. Lambrecht, R.B. Wehrspohn, Photonic crystal gas sensors, Proc. SPIE 5511 (2004) 61–70.
[2] I. Puscasu, E. Johnson, M. Pralle, M. McNeal, J. Daly, A. Greenwald, Photonic crystals enable infrared gas sensors, Proc. SPIE 5515 (2004) 58–66.
[3] A. Lambrechta, S. Hartwig, S.L. Schweizer, R.B. Wehrspohnb, Miniature infrared gas sensors using photonic crystals, Proc. SPIE 6480 (2007) 64800D1–6480010D6480010.
[4] W. Xiaoling, L. Naiguang, Z. Jun, J. Guofan, An ultracompact refractive index gas-sensor based on photonic crystal microcavity, Proc. SPIE 6831 (2007) 68310D1–683106D683106.
[5] V.M. Agranovich, D.L. Mills, Surface Polaritons—Electromagnetic Waves at Surfaces and Interfaces, North-Holland, Amsterdam, 1982.
[6] E. Kretschmann, H. Raether, Radiative decay of non radiative surface plasmons excited by light, Naturforschung A 23 (1968) 2135.
[7] B. Liedberg, C. Nylander, I. Lundström, Surface plasmon resonance for gas detection and biosensing, Sens. Actuators B 4 (1983) 299.
[8] J.L. Melendez, R. Carr, D.U. Bartholomew, K.A. Kukanskis, J. Elkind, S.S. Yee, C.E. Furlong, R.G. Woodbury, A commercial solution for surface plasmon sensing, Sens. Actuators B 35 (1996) 212.
[9] L.M. Zhang, D. Uttamchandani, Optical chemical sensing employing surface plasmon resonance, Electron. Lett. 23 (1988) 1469.
[10] A.V. Kabashin, P. Nikitin, Surface plasmon resonance interferometer for bio- and chemical-sensors, Opt. Commun. 150 (1998) 5.
[11] A.N. Grigorenko, P. Nikitin, A.V. Kabashin, Phase jumps and interferometric surface plasmon resonance imaging, Appl. Phys. Lett. 75 (1999) 3917.
[12] J. Homola, Surface Plasmon Resonance Based Sensors, Springer, New York, 2006.
[13] G.G. Nenninger, P. Tobiska, J. Homola, S.S. Yee, Long-range surface plasmons for high-resolution surface plasmon resonance sensors, Sens. Actuators B 74 (2001) 145–151.
[14] N.J. Tao, S. Boussaad, W.L. Huang, R.A. Arechabaleta, J. D'Agnese, High resolution surface plasmon resonance spectroscopy, Rev. Sci. Instrum. 70 (1999) 4656–4660.
[15] A.G. Brolo, R. Gordon, B. Leathem, K.L. Kavanagh, Surface plasmon sensor based on the enhanced light transmission through arrays of nanoholes in gold films, Langmuir 20 (2004) 4813–4815.
[16] K.A. Tetz, L. Pang, Y. Fainman, High-resolution surface plasmon resonance sensor based on linewidth-optimized nanohole array transmittance, Opt. Lett. 31 (2006) 1528–1530.
[17] S. Xiao, N.A. Mortensen, M. Qiu, Enhanced transmission through arrays of subwavelength holes in gold films coated by a finite dielectric layer, J. Eur. Opt. Soc. 2 (2007), 07009-1–07009-4.
[18] T.W. Ebbesen, H.J. Lezec, H.F. Ghaemi, T. Thio, P.A. Wolff, Nature 391 (1998) 667–669.
[19] http://ab-initio.mit.edu/wiki/index.php/Meep.
[20] A. Vial, A.S. Grimault, D. Macias, D. Barchiesi, M.L. Chapelle, Improved analytical fit of gold dispersion: application to the modeling of extinction spectra with a finite-difference time-domain method, Phys. Rev. B 71 (2005) 085416–085422.
[21] A.V. Kabashin, P.I. Nikitin, Interferometer based on a surface-plasmon resonance for sensor applications, Quan. Electron. 27 (1997) 653–654.
[22] S. Shen, T. Liu, J. Guo, Optical phase-shift detection of surface plasmon resonance, Appl. Opt. 37 (1998) 1747–1751.
[23] V.E. Kochergin, A.A. Beloglazov, M.V. Valeiko, P.I. Nikitin, Phase properties of a surface-plasmon resonance from the viewpoint of sensor applications, Quan. Electron. 28 (1998) 444–448.
[24] A.V. Kabashin, V.E. Kochergin, A.A. Beloglazov, P.I. Nikitin, Phase-polarization contrast for surface plasmon resonance biosensors, Biosens. Bioelectron. 13 (1998) 1263–1269.
[25] P.I. Nikitin, A.A. Beloglazov, V.E. Kochergin, M.V. Valeiko, T.I. Ksenevich, Surface plasmon resonance interferometry for biological and chemical sensing, Sens. Actuators B 54 (1999) 43–50.
[26] A.V. Kabashin, V.E. Kochergin, P.I. Nikitin, Surface plasmon resonance bio- and chemical sensors with phase-polarization contrast, Sens. Actuators B 54 (1999) 51–56.
[27] A.N. Grigorenko, A.A. Beloglazov, P.I. Nikitin, C. Kuhne, G. Steiner, R. Salzer, Dark-field surface plasmon resonance microscopy, Opt. Commun. 174 (2000) 151–155.
[28] P.I. Nikitin, A.N. Grigorenko, A.A. Beloglazov, M.V. Valeiko, A.I. Savchuk, O.A. Savchuk, Surface plasmon resonance interferometry for micro-array biosensing, Sens. Actuators A 85 (2000) 189–193.
[29] Y. Xinglong, W. Dingxin, Y. Zibo, Simulation and analysis of surface plasmon resonance biosensor based on phase detection, Sens. Actuators B 91 (2003)

285–290.
[30] C.M. Wu, Z.C. Jian, S.F. Joe, L.B. Chang, High-sensitivity sensor based on surface plasmon resonance and heterodyne interferometry, Sens. Actuators B 92 (2003) 133–136.
[31] C.M. Wu, M.C. Pao, Sensitivity-tunable optical sensors based on surface plasmon resonance and phase detection, Opt. Express 12 (2004) 3509–3514.
[32] A.K. Sheridan, R.D. Harris, P.N. Bartlett, J.S. Wilkinson, Phase interrogation of an integrated optical SPR sensor, Sens. Actuators B 97 (2004) 114–121.
[33] S.Y. Wu, H.P. Ho, W.C. Law, C. Lin, S.K. Kong, Highly sensitive differential phase-sensitive surface plasmon resonance biosensor based on the Mach–Zehnder configuration, Opt. Lett. 29 (2004) 2378–2380.
[34] Y. Xinglong, W. Dingxin, W. Xing, D. Xiang, L. Wei, Z. Xinsheng, A surface plasmon resonance imaging interferometry for protein micro-array detection, Sens. Actuators B 108 (2005) 765–771.
[35] Y.D. Su, S.J. Chen, T.L. Yen, Common path phase shift interferometry surface plasmon resonance imaging system, Opt. Lett. 30 (2005) 1488–1490.
[36] B. Ran, S.G. Lipson, Comparison between sensitivities of phase and intensity detection in surface plasmon resonance, Opt. Express 14 (2006) 5641–5650.
[37] T. König, M. Weidemüller, A. Hemmerich, Real-time phase-shift detection of the surface plasmon resonance, Appl. Phys. B 93 (2008) 545–549.

Biography

Dr. Maksim Skorobogatiy has received his BSc degree in physics from Rochester Institute of Technology, Rochester, USA (1995); MSc in physics from McGill University, Montréal, Canada (1997); MSc in electrical engineering and computer science from Massachusetts Institute of Technology (MIT), Cambridge, USA (2000); PhD in physics also from MIT in 2001. During 2001–2003 he was heading a theory and simulations group at MIT startup OmniGuide Inc., where he was working on commercialization of the hollow photonic bandgap fiber technology for delivery of high power laser beams. Since 2003, he is an associate professor and a Canada Research Chair in Micro- and Nano-Photonics at Ecole Polytechnique de Montréal/University de Montréal, Canada. His current fields of interest include design and fabrication of photonic crystal fibers for sensing and telecommunications, as well as the general fields of plasmonics, and nano-photonics.